Micro-Nano-Structured Fe2O3:Ti/ZnFe2O4 Heterojunction Films for Water Oxidation

6 AUTHORS, INCLUDING:

Shulin Ji

Chinese Academy of Sciences

40 PUBLICATIONS **273** CITATIONS

# Micro-Nano-Structured Fe_2O_3:Ti/$ZnFe_2O_4$ Heterojunction Films for Water Oxidation

Chunhui Miao, Shulin Ji, Guoping Xu, Guodong Liu, Lide Zhang, and Changhui Ye*

Anhui Key Laboratory of Nanomaterials and Technology and Key Laboratory of Materials Physics, Institute of Solid State Physics, Chinese Academy of Sciences, Hefei 230031, China

S *Supporting Information*

ABSTRACT: Iron(III) oxide photoelectrodes show promise in water oxidation applications. In this study, micro-nano-structured hematite films are synthesized, and Ti ions are doped to improve photoelectric conversion efficiency. The photocurrent increases for enhanced electrical conductivity. Further enhanced photocurrent is achieved for Fe_2O_3:Ti/$ZnFe_2O_4$ heterojunction electrodes. Cyclic voltammograms combined with optical absorbance examinations demonstrate that the conduction and valence band edges of $ZnFe_2O_4$ shift from those of Ti doped Fe_2O_3 to the negative direction, which facilitates the

efficient separation of electron–hole pairs at the Fe_2O_3:Ti/$ZnFe_2O_4$ interface. These findings demonstrate that, by doping hematite and by engineering the interface between the hematite and the electrolyte, charge separation can be effectively promoted and photocurrent density can be dramatically increased.

KEYWORDS: *micro-nano-structure, Ti-doped hematite, heterojunction electrode, water oxidation, $ZnFe_2O_4$, electrochemical impedance*
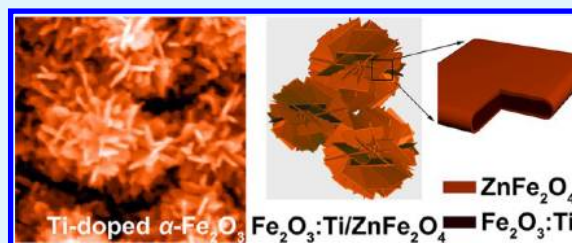
1. INTRODUCTION

Hematite has several advantages as a semiconducting material for water oxidation:[1−3] it can utilize approximately 40% of incident solar radiation for its optical band gap of ~2 eV;[4] it is stable under an alkaline condition;[5] the position of its valence band is suitable for oxygen evolution.[6] However, the water oxidation activity of hematite is limited by several key factors, such as relatively poor absorptivity,[7] short excited-state lifetime (approximately 10^{-12} s),[1] poor oxygen evolution reaction kinetics,[8] short hole diffusion length (2−4 nm),[9,10] and low electron mobility.[4,11] These factors lead to poor water oxidation efficiency.

Many researchers have devoted their efforts to the rational design of photoanodes at a micro-nano scale to address the problem of short diffusion length of photogenerated holes,[12−14] which were believed to enhance the harvesting of photo-generated holes due to their large surface area and feature size comparable to the hole diffusion length. In addition, an effective method for improving the conductivity of hematite could be obtained by intentional doping. The enhanced electrical conductivity can extend the lifetime of the charge carriers, reduce the recombination of the electron–hole pairs, and improve the power conversion efficiency. Ti doping has been shown to increase the conductivity of hematite both theoretically and experimentally.[15,16] Oxygen plasma-assisted molecular beam epitaxy,[17] reactive ballistic deposition along with glancing angle deposition,[15] spin-coating,[18] spray pyrolysis,[3] atmospheric pressure chemical vapor deposition,[3] and radio frequency magnetron sputtering[19] were employed to fabricate the Ti-doped hematite films. In this work, we prepared micro-nano-structured hematite electrodes in an acid solution

using a simple hydrothermal method. TiCl$_4$ was used as a precursor to introduce Ti ions into hematite. The as-synthesized structures were composed of pine nut-like balls assembled by nanosheets with thickness comparable to the hole diffusion length.

Heterojunction structures have been fabricated to further improve power conversion efficiency by enhancing the separation of electron–hole pairs.[20−24] Recently, some materials have been applied to prepare heterojunction structures together with hematite to enhance the photoelectric conversion efficiency, such as cobalt phosphate,[21] TiO$_2$,[22] and SrTiO$_3$.[23] Compared to those materials, $ZnFe_2O_4$ is stable in weak acidic or alkaline conditions,[24] and the conduction and valence band edge positions of $ZnFe_2O_4$ are more negative than those of α-Fe_2O_3; therefore, Fe_2O_3:Ti/$ZnFe_2O_4$ heterojunction structure can enhance the separation of electron–hole pairs more effectively than α-Fe_2O_3:Ti. In this paper, we report on the synthesis, characterization, and water oxidation performance of α-Fe_2O_3:Ti and Fe_2O_3:Ti/$ZnFe_2O_4$ heterojunction photoanodes.

2. EXPERIMENTAL SECTION

2.1. Synthesis of Pure α-Fe_2O_3 and α-Fe_2O_3:Ti Photoanodes. An aqueous solution (19 mL) containing 0.1 M FeCl$_3$, 0.5 M NaNO$_3$, and 1 mL of ethanol was sealed in a 50 mL polytetrafluoroethylene liner. The liner was put into a self-sealing autoclave and heated at 100 °C for 12 h. Fluorine-doped tin oxide (FTO)-coated glass was placed

in the liner with the FTO side facing the wall of the liner. Instead of pure ethanol, 1 mL of $TiCl_4$ ethanol solution was added into the precursor solution to dope the Ti ions into the hematite. After the reaction, the film formed on the FTO was thoroughly rinsed with deionized water and annealed at 550 °C for 2 h in the atmosphere to obtain the desired phase (α-Fe_2O_3). The notations for the samples (volume ratio of $TiCl_4$ in ethanol solution) were PF (0%), TF-1 (0.5%), TF-2 (1%), and TF-3 (2%), respectively.

2.2. Preparation of Fe_2O_3:Ti/$ZnFe_2O_4$ Heterojunction Photoanodes. α-Fe_2O_3:Ti/$ZnFe_2O_4$ heterojunction electrodes were prepared by dropping 20 μL ethanol solutions of 0.2 M $Zn(NO_3)_2$ onto the α-Fe_2O_3:Ti electrodes (TF-3; the area of the Ti-doped hematite is approximately 2 cm × 1.4 cm).[24] The resulting samples were annealed at 550 °C for 10 h in the atmosphere. These electrodes were then soaked in 1 M NaOH solution at room temperature for 12 h to remove the remaining ZnO on the surface of the electrodes. These samples were denoted as ZFO-1 ($Zn(NO_3)_2$ treated once), ZFO-2 ($Zn(NO_3)_2$ treated twice), and ZFO-3 ($Zn(NO_3)_2$ treated thrice), respectively.

2.3. Characterizations. The characterization experiments were conducted at room temperature. The crystalline phase of the samples was identified by X-ray diffraction (XRD) using a Philips X'Pert Pro MPD with Cu Kα (λ = 1.5406 Å) radiation. The morphology of the samples was determined by field emission scanning electron microscopy (FESEM; FEI Sirion-200) coupled with energy dispersive X-ray analysis (EDX). The crystal structure of the samples was determined by high-resolution transmission electron microscopy (HRTEM; JEOL JEM-2010, 200 KV). Optical absorption measurements were performed using a UV−visible absorption spectrometer (Shimadzu UV 3600). X-ray photoelectron spectra (XPS) were recorded using an electron spectrometer fitted with an Al Kα source (Thermo ESCALAB 250, soft X-ray source at 1486.6 eV).

Electrochemical impedance spectroscopy, cyclic voltammetry (CV), and photocurrent measurements were conducted using an electrochemical workstation (Zahner IM6ex) in a three-electrode electrochemical system with 1 M NaOH electrolyte (back-side illumination). Platinum foil was used as the counter electrode. The measured potential vs. Ag/AgCl (sat. KCl) reference electrode was converted to the reversible hydrogen electrode (RHE) scale according to the following Nernst equation:

$$E_{RHE} = E_{Ag/AgCl} + 0.059 \, pH + E^{o}_{Ag/AgCl}$$

where E_{RHE} is the converted potential vs. RHE, $E^{o}_{Ag/AgCl}$ = 0.1976 V at 25 °C, and $E_{Ag/AgCl}$ is the experimentally measured potential against the Ag/AgCl (sat. KCl) reference electrode.

3. RESULTS AND DISCUSSION

3.1. Ti-Doped α-Fe_2O_3 Electrodes. *3.1.1. Morphology, Phase, and Structure Characterizations.* The hydrothermal growth of α-Fe_2O_3 nanostructured films at 100 °C is due to the precipitation of Fe^{3+} ions in a weak acid solution (pH ∼ 1.25−1.5)[25] followed by annealing at 550 °C. Figure 1 shows the XRD patterns of pure and Ti-doped α-Fe_2O_3 electrodes. All four spectra could be assigned to α-Fe_2O_3. After subtracting the diffraction peaks originating from the FTO substrate, the absence of FeOOH diffraction peaks indicates the complete conversion of FeOOH to α-Fe_2O_3. The influence of the introduction of Ti-dopant on the interplanar spacing of hematite was determined by adopting a much slower scanning speed. The XRD patterns are shown in Figure S1, Supporting Information. With the increased amount of $TiCl_4$ precursor, the interplanar spacings of the (104) and (110) lattice planes decrease, as shown in Table S1, Supporting Information. These findings are in agreement with previously reported results,[4,11,26] considering that the ionic radii for six-coordinate Fe^{3+} and Ti^{4+} are 0.65 and 0.61 Å, respectively.[26,27]
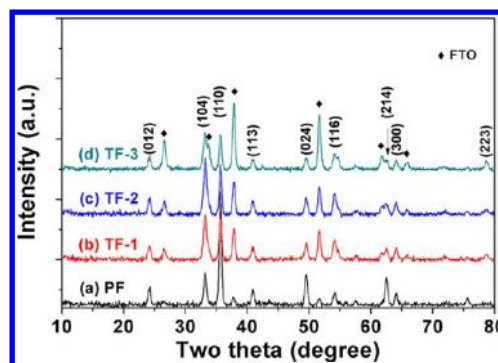

Figure 1. X-ray diffraction patterns of (a) PF, (b) TF-1, (c) TF-2, and (d) TF-3.

Figure 2 shows the SEM images (top view) of pure and Ti-doped α-Fe_2O_3 electrodes. Figure 2a indicates that the PF
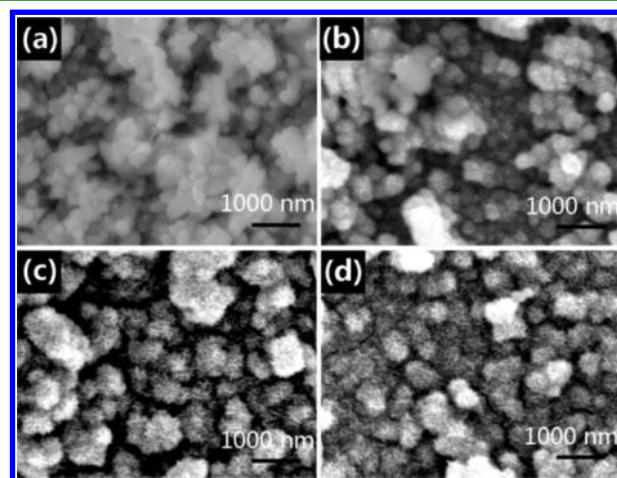
Figure 2. SEM images of pure and Ti-doped α-Fe_2O_3 films. (a) PF, (b) TF-1, (c) TF-2, and (d) TF-3.

electrode is covered by particles with diameters of approximately 300 nm. The introduction of $TiCl_4$ results in the transformation of the film to micro-nano structures comprising pine nut-like balls. The micro-nano morphology was confirmed by the enlarged SEM image (TF-3) shown in Figure 3a, where nanosheets can be clearly observed. The HRTEM image and the selected area electron diffraction (SAED) pattern of TF-3
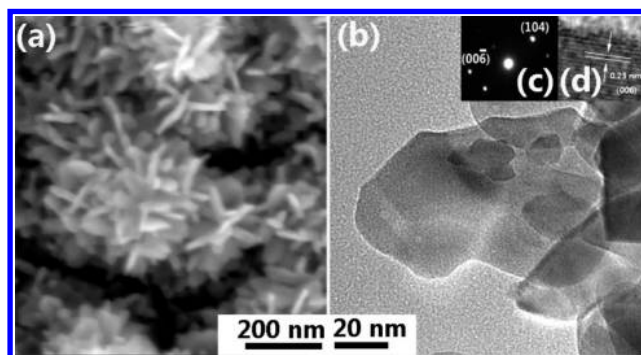

Figure 3. (a) SEM image of TF-3. (b) TEM and (d) HRTEM images of TF-3 scrapped from the substrate. (c) The electron diffraction patterns of TF-3.

4429

dx.doi.org/10.1021/am3011466 | *ACS Appl. Mater. Interfaces* 2012, 4, 4428−4433

further indicate that the as-prepared samples are α-Fe_2O_3 (Figure 3).

XPS analysis was performed on the samples to further determine the amount of Ti and to confirm the incorporation of Ti ions into hematite. XPS data showed that the Ti atomic ratios of TF-1, TF-2, and TF-3 are 0.82%, 1.05%, and 2.20%, respectively. The concentration of Ti ions of these Ti-doped hematite increases with the amount of $TiCl_4$ added, a result consistent with the XRD analysis.

XPS performed on TF-3 reveals that the Fe 2p spectrum, shown in Figure 4a, possesses the typical $2p_{1/2}$ and $2p_{3/2}$ peaks
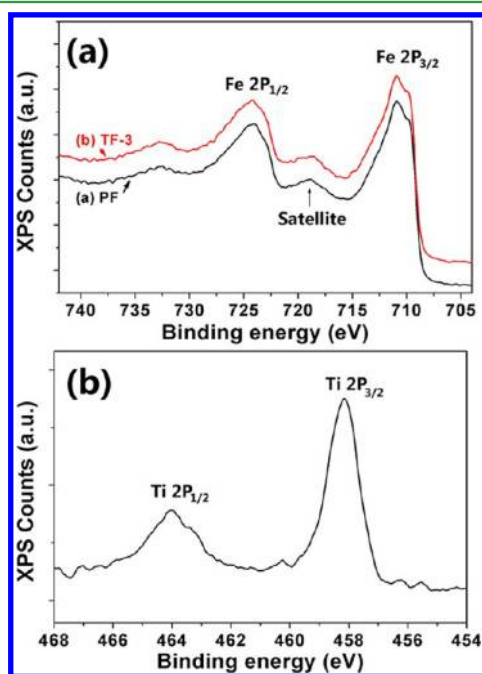

Figure 4. XPS curves of (a) Fe 2p of PF (black line) and Fe 2p of TF-3 (red line); (b) Ti 2p recorded from TF-3.

of Fe^{3+}.[25] The lack of observable Fe^{2+} satellite peaks at 715 or 730 eV indicate the absence of Fe^{2+} on the electrode surface. Figure 4b indicates that Ti is in the +4 state, as proven by the $2p_{1/2}$ and $2p_{3/2}$ peaks present in the Ti 2p spectrum at 458.1 and 463.8 eV, respectively. These values agree with the typical 2p binding energy of Ti^{4+} ions.[28,29] A comparison with the reported result for TiO_2 (458.5 eV for $2p_{3/2}$ binding energy),[29,30] a red shift of about 0.4 eV occurs, indicating the different microenvironment of Ti^{4+} ions in Ti-doped α-Fe_2O_3 from that of pure TiO_2.

3.1.2. Positions of the Conduction Band and the Valence Band. Figure 5 shows the light absorption spectra of pure and Ti-doped α-Fe_2O_3 electrodes. Each spectrum shows features typical of α-Fe_2O_3 films with an absorption onset of approximately 595 nm. The band gap was calculated as approximately 2.05 eV (inset in Figure 5). No shift of the absorption onset of α-Fe_2O_3 due to the Ti-dopant could be observed.

The electrons transferring through the conduction band and valence band are expected to present a cathodic and an anodic peak, respectively, in the cyclic voltammogram curves.[31,32] For our experiments measured in a three-electrode electrochemical cell, cathodic peaks corresponding to the conduction band position of α-Fe_2O_3 electrode is the only observed peak. The valence band position could be defined combined with the
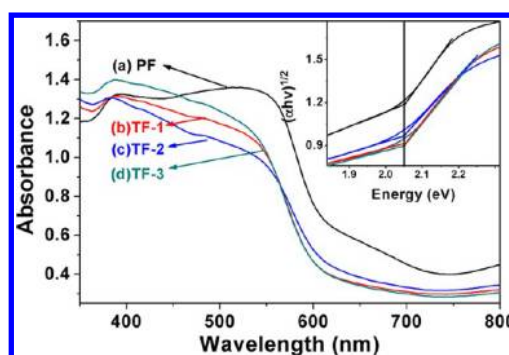
Figure 5. UV−vis absorption spectra of pure and Ti-doped α-Fe_2O_3 electrodes: (a) PF, (b) TF-1, (c) TF-2, and (d) TF-3. The inset shows the band gap of pure and Ti-doped α-Fe_2O_3 electrodes.

band gap value obtained from optical absorption analysis. Although theoretical calculations indicate that the conduction band of Ti-doped hematite would shift to a slightly positive position,[16] our results showed that the surface conduction band (E_{sc}) and valence band (E_{sv}) positions of Ti-doped α-Fe_2O_3 do not shift compared with pure hematite (Figure 6). This result is in agreement with the result reported by Wang et al.[33]
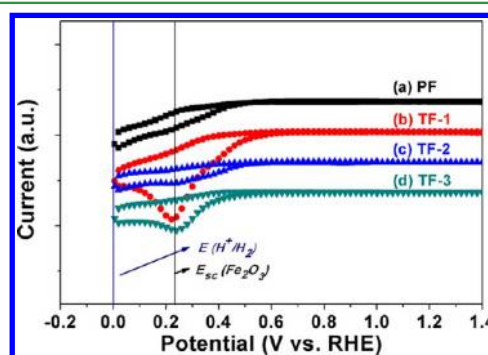
Figure 6. Cyclic voltammograms recorded on pure and Ti-doped α-Fe_2O_3 electrodes. (a) PF, (b) TF-1, (c) TF-2, and (d) TF-3.

3.1.3. Photocurrent and Mott−Schottky Plots. The performance of Ti-doped α-Fe_2O_3 films was investigated as a function of the concentration of Ti-dopants. Figure 7 compares the linear sweeps of pure and Ti-doped α-Fe_2O_3 films. The photocurrent densities of α-Fe_2O_3 film increase with the concentration of the Ti-dopants. The photocurrent reaches a maximal value when the concentration of Ti-dopants in hematite is 2.20%. TF-1, TF-2, and TF-3 have similar morphologies; however, compared to TF-1, the photocurrent onset potential of TF-2 and TF-3 decreases as the concentration of Ti-dopants increases (Figure 7a). Therefore, improvement of the photocurrent at a lower bias voltage could be achieved. A similar trend was observed for Si- and Ti-doped hematite.[7,33] The impact of morphology on the photocurrent was also studied. When the hydrothermal temperature was increased to 150 °C with the other conditions the same to that for TF-3, nanospheres were produced. Figure S2a, Supporting Information, shows the SEM image of this sample, for which the photocurrent decreased compared to TF-3 (Figure S2b, Supporting Information), indicating that an appropriate morphology was essential for harvesting the sunlight with a high efficiency.
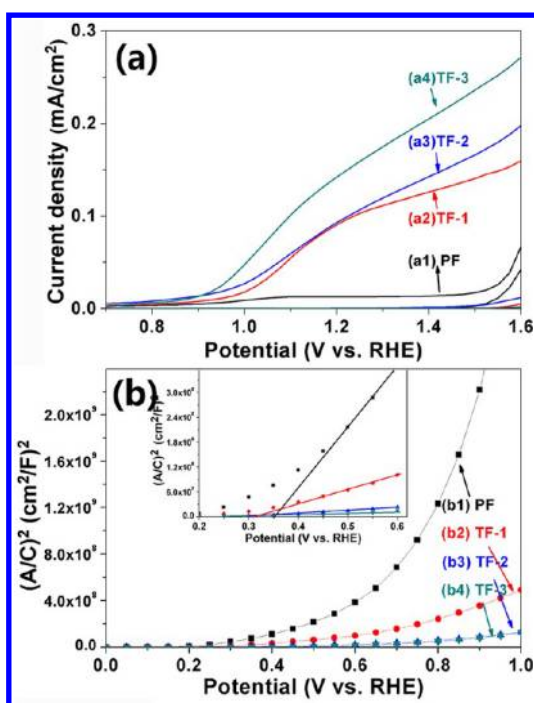
Figure 7. (a) Photocurrent−voltage characteristics in 1 M NaOH under AM 1.5 G illumination and in darkness: (a1) PF, (a2) TF-1, (a3) TF-2, and (a4) TF-3. (b) M-S Plots of pure and Ti-doped α-Fe_2O_3 electrodes: (b1) PF, (b2) TF-1, (b3) TF-2, and (b4) TF-3. The inset in (b) is an enlarged portion of (b).

Mott−Schottky Plots (M-S plots) were employed to study the electronic properties of pure and Ti-doped hematite electrodes. The films were analyzed in the dark in 1 M NaOH. M-S plots for the samples were recorded at 1000 Hz. As shown in Figure 7b, nonlinear behavior was observed for pure and Ti-doped hematite electrodes. The reason for the nonlinearity can be attributed to the presence of deep levels or surface states.[34,35] The slope in the quasi-linear regions of the M-S plots near the flat-band potential (E_{fb}) where the depletion layer remains very thin was used to calculate the donor concentrations of the films as 2.72×10^{18} cm^{-3}, 1.48×10^{19} cm^{-3}, 2.84×10^{19} cm^{-3}, and 9.71×10^{19} cm^{-3} for the four films, respectively (Table S2, Supporting Information). The flat-band potential shifted toward negative direction with the increase of the donor concentration, which can be interpreted as a consequence of the modified donor concentration and the related upward shift of the Fermi level caused by Ti doping. Our experimental results indicate that the carrier density increases with the concentration of the Ti-dopants. The enhanced electrical conductivity can extend the lifetime of the charge carriers, reduce the recombination of the electron−hole pairs, and improve the water oxidation efficiency.[16]

EIS analysis was adopted to further understand the role of Ti-dopants played in water oxidation processes.[36] The electrical analog we used to fit the EIS data was shown in Figure S3a, Supporting Information. The resistance accounting for surface state trapping electrons from the conduction band and holes from the valence band, acting as a recombination center, is given by $R_{trapping}$. Surface states affect the charge transfer of holes to the donor species in solution, which could be described as a resistance $R_{ct,trap}$. The trap-state capacitance was denoted as C_{trap}, and the space charge capacitance (C_{sc}) and the series connection of the Helmholtz capacitance (C_h) have been

lumped into C_{bulk}. Finally, R_S is the series resistance of the cell.[36] In our present work, a constant phase element (CPE) was used to obtain a better fit, and the effective capacitance of a CPE is calculated by the method suggested by Brug et al.[37,38] Nyquist plots and Bode plots for PF, TF-1, TF-2, and TF-3 electrodes measured at 1.3 V vs RHE under 1 sun illumination are shown in Figure S3, Supporting Information, and the equivalent circuit parameters obtained from fitting EIS data are summarized in Table S3, Supporting Information. R_s decreased and C_{bulk} increased with the concentration of the Ti-dopants, which coincides with the M-S plots showed in Figure 7b. Compared to PF, $R_{ct,trap}$ and $R_{trapping}$ of Ti-doped hematite decrease dramatically and C_{trap} increases with the concentration of the Ti-dopants. Because the water oxidation reaction involves the participation of four holes, photogenerated holes have to be stored in intermediate states.[36,39] Increased C_{trap} means more holes could be stored in the surface state. The decrease of $R_{ct,trap}$ and $R_{trapping}$ indicates that the photocurrent enhancement of Ti-doped films is due to the facilitated charge transfer of holes to the donor species in solution.

3.2. Fe_2O_3 (Ti-Doped)/$ZnFe_2O_4$ Heterojunction Electrodes. *3.2.1. Morphology, Phase, and Positions of the Conduction Band and the Valence Band.* Figure 8a−c shows
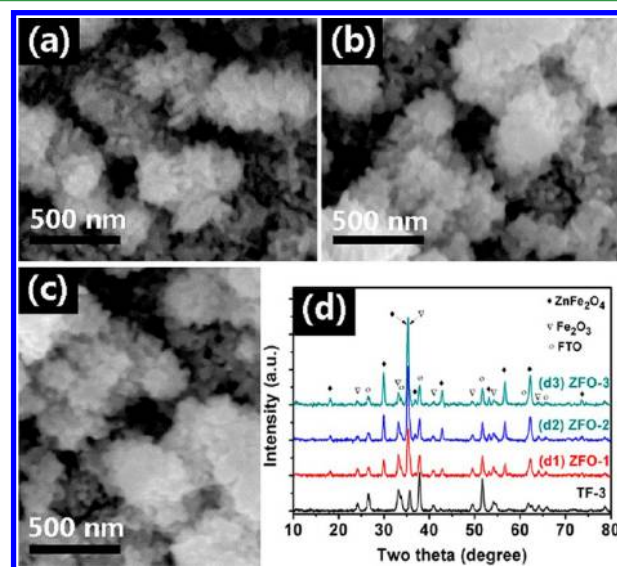
Figure 8. SEM images for Fe_2O_3:Ti/$ZnFe_2O_4$ heterojunction films: (a) ZFO-1, (b) ZFO-2, and (c) ZFO-3. (d) the XRD patterns of (d1) ZFO-1, (d2) ZFO-2, and (d3) ZFO-3.

the SEM (top view) images of Fe_2O_3:Ti/$ZnFe_2O_4$ electrodes ZFO-1, ZFO-2, and ZFO-3. The nanosheets overgrow and the film gets smoothened with increasing $Zn(NO_3)_2$ treatments. Figure 8d demonstrates that the intensity of the diffraction peaks originating from $ZnFe_2O_4$ increases, whereas the intensity of the diffraction peaks originating from α-Fe_2O_3 decreases with the $Zn(NO_3)_2$ treating times. This result suggests that more Fe_2O_3 transformed to $ZnFe_2O_4$. EDX analysis proved the same trend, as shown in Figure S4 and Table S4, Supporting Information.

Figure 9a shows the light absorbance of TF-3 and Fe_2O_3:Ti/$ZnFe_2O_4$ electrodes. The absorbance of $Zn(NO_3)_2$ treated electrodes declines compared to the untreated sample, because of the increased reflectance of the smoothened films. However, the absorption onset of $Zn(NO_3)_2$ treated electrodes remains at
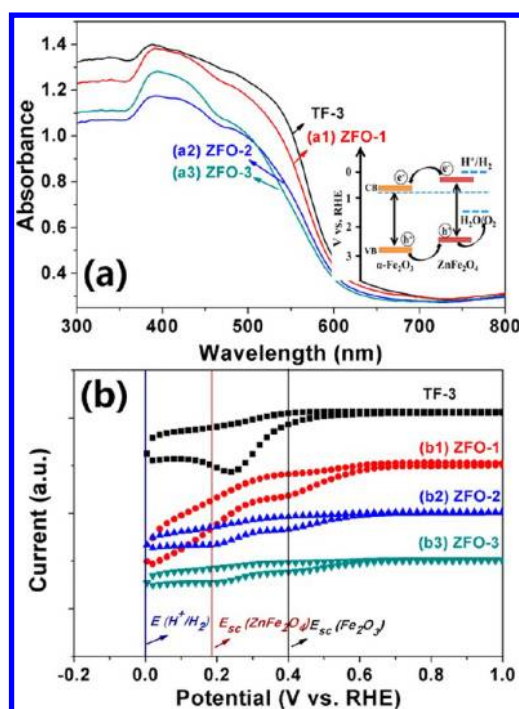
Figure 9. (a) UV−vis spectra of (a1) ZFO-1, (a2) ZFO-2, and (a3) ZFO-3. (b) Cyclic voltammograms of (b1) ZFO-1, (b2) ZFO-2, and (b3) ZFO-3. The inset in (a) shows the band positions of Ti-doped α-Fe$_2$O$_3$ and ZnFe$_2$O$_4$ electrodes at pH 13.6.

Figure 10. (a) Photocurrent−voltage characteristics in 1 M NaOH under AM 1.5 G illumination and in darkness at a scan rate of 25 mV/s. (a1) ZFO-1, (a2) ZFO-2, and (a3) ZFO-3. (b) M-S Plots of (b1) ZFO-1, (b2) ZFO-2, and (b3) ZFO-3.

the same position compared with TF-3, which is because the band gap of ZnFe$_2$O$_4$ is close to that of α-Fe$_2$O$_3$.[40] The CV examination on Zn(NO$_3$)$_2$ treated electrodes revealed that the cathodic peaks corresponding to the conduction band positions for ZnFe$_2$O$_4$ electrodes is 210 mV higher than that corresponding to α-Fe$_2$O$_3$, in agreement with previously reported results (Figure 9b).[40] The surface conduction band (E_{sc}) and valence band (E_{sv}) positions of both α-Fe$_2$O$_3$ and ZnFe$_2$O$_4$ were estimated, as shown in the inset in Figure 9a, where the conduction and valence band edge positions of ZnFe$_2$O$_4$ are ideally offset from those of α-Fe$_2$O$_3$. This offset suggests that combining α-Fe$_2$O$_3$ and ZnFe$_2$O$_4$ will promote the separation of electron−hole pairs generated in both α-Fe$_2$O$_3$ and ZnFe$_2$O$_4$.

The photocurrents of Fe$_2$O$_3$:Ti/ZnFe$_2$O$_4$ heterojunction electrodes were measured with sweeping potential. Figure 10a shows that the photocurrent of the ZFO-1 heterojunction electrode is enhanced compared to that of the TF-3 electrode. This enhancement originates from the gradual establishment of the depletion layer in the heterojunction, as proven by CVs. However, treating TF-3 with Zn(NO$_3$)$_2$ further leads to a decrease of photocurrent, which might be due to the decrease of the surface roughness as shown in Figure 8. Another possible reason is that the increased thickness of ZnFe$_2$O$_4$ leads to the increase of the bulk recombination. Equivalent circuit parameters obtained by fitting EIS data of ZFO-1, ZFO-2, and ZFO-3 are shown in Table S3, Supporting Information. ZFO-1 possess the minimal $R_{ct,trap}$ and $R_{trapping}$ and the maximal C_{trap} values, confirming our suggestion that the heterojunction could enhance the separation of electron−hole pairs and suppress the recombination. The photocurrent onset potential of ZFO-1 shifts to negative direction compared to TF-3; however, with increased thickness of ZnFe$_2$O$_4$, the photocurrent onset potential moves toward the positive direction,
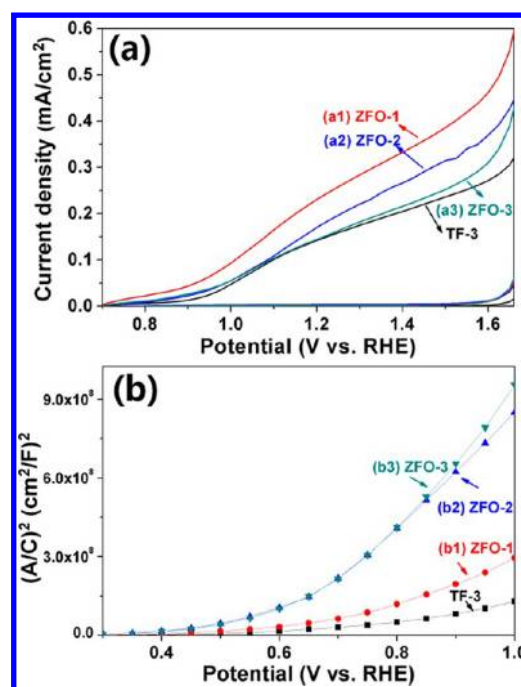
which is another piece of evidence of the increased surface recombination after an optimum amount of ZnFe$_2$O$_4$.[39]

M-S plots for the Zn(NO$_3$)$_2$ treated films were also recorded at 1000 Hz and shown in Figure 10b. The larger slope with the Zn(NO$_3$)$_2$ treatment compared to TF-3 sample indicates that the carrier density of Fe$_2$O$_3$ does not change toward a more favorable direction after the treatment. Thus, the promoted separation of electron−hole pairs generated in Ti-doped α-Fe$_2$O$_3$ and ZnFe$_2$O$_4$ is the most possible reason for the enhanced photocurrent.

4. CONCLUSIONS

Micro-nano-structured hematite films were synthesized via a simple hydrothermal method. Ti-dopants enhanced the electrical conductivity, facilitated the separation and transport of electrons and holes, and led to the increase of the photocurrent. Further enhanced electron−hole separation was achieved by forming a Fe$_2$O$_3$:Ti/ZnFe$_2$O$_4$ heterojunction photoelectrode. The improvement of the electron−hole separation by the heterojunction structure further improved the photocurrent density. The design of this heterojunction photoelectrode will have potential applications for producing highly efficient water-splitting materials.

■ ASSOCIATED CONTENT

Ⓢ Supporting Information

Five additional figures and four tables elaborating on experimental results. This information is available free of charge via the Internet at http://pubs.acs.org/.

■ AUTHOR INFORMATION

Corresponding Author
*E-mail: chye@issp.ac.cn.

■ REFERENCES

(1) Cherepy, N. J.; Liston, D. B.; Lovejoy, J. A.; Deng, H. M.; Zhang, J. Z. *J. Phys. Chem. B* **1998**, *102*, 770−776.

(2) Kay, A.; Cesar, I.; Grätzel, M. *J. Am. Chem. Soc.* **2006**, *128*, 15714−15721.

(3) Cesar, I.; Kay, A.; Gonzalez, M. J. A.; Grätzel, M. *J. Am. Chem. Soc.* **2006**, *128*, 4582−4583.

(4) Tang, H. W.; Yin, W. J.; Matin, M. A.; Wang, H. L.; Deutsch, T.; Al-Jassim, M. M.; Turner, J. A; Yan., Y. F. *J. Appl. Phys.* **2012**, *111*, 073502.

(5) Kennedy, J. H.; Anderman, M. J. *J. Electrochem. Soc.* **1983**, *130*, 848−852.

(6) Lindgren, T.; Wang, H. L.; Beermann, N.; Vayssieres, L.; Hagfeldt, A.; Lindquist, S. E. *Sol. Energy Mater. Sol. Cells* **2002**, *71*, 231−243.

(7) Cesar, I.; Sivula, K.; Kay, A.; Zboril, R.; Grätzel, M. *J. Phys. Chem. C* **2009**, *113*, 772−782.

(8) Dareedwards, M. P.; Goodenough, J. B.; Hamnett, A.; Trevellick, P. R. *J. Chem. Soc., Faraday Trans.* **1983**, *79*, 2027−2041.

(9) Sivula, K.; Zboril, R.; Le Formal, F.; Robert, R.; Weidenkaff, A.; Tucek, J.; Frydrych, J.; Grätzel, M. *J. Am. Chem. Soc.* **2010**, *132*, 7436−7444.

(10) Duret, A.; Grätzel, M. *J. Phys. Chem. B* **2005**, *109*, 17184−17191.

(11) Huda, M.; Walsh, A.; Yan, Y. F.; Wei, S. H.; Al-Jassim, M. M. *J. Appl. Phys.* **2010**, *107*, 123712.

(12) Brillet, J.; Grätzel, M.; Sivula, K. *Nano Lett.* **2010**, *10*, 4155−4160.

(13) Beermann, N.; Vayssieres, L.; Lindquist, S. E.; Hagfeldt, A. *J. Electrochem. Soc.* **2000**, *147*, 2456−2461.

(14) Wang, H.; Deutsch, T.; Turner, J. A. *J. Electrochem. Soc.* **2008**, *155*, F91−F96.

(15) Hahn, N. T.; Mullins, C. B. *Chem. Mater.* **2010**, *22*, 6474−6482.

(16) Meng, X. Y.; Qin, G. W.; Li, S.; Wen, X. H.; Ren, Y. P.; Pei, W. L.; Zuo, L. *Appl. Phys. Lett.* **2011**, *98*, 112104.

(17) Droubay, T.; Rosso, K. M.; Heald, S. M.; McCready, D. E.; Wang, C. M.; Chambers, S. A. *Phys. Rev. B* **2007**, *75*, 104412.

(18) Lian, X. J.; Yang, X.; Liu, S. J.; Xu, Y.; Jiang, C. P.; Chen, J. W.; Wang, R. L. *Appl. Surf. Sci.* **2012**, *258*, 2307−2311.

(19) Tang, H. W.; Matin, M. A.; Wang, H. L.; Deutsch, T.; Al-Jassim, M.; Turner, J.; Yan, Y. F. *J. Appl. Phys.* **2011**, *110*, 123511.

(20) Yang, C. Y.; Wang, W. D.; Shan, Z. C.; Huang, F. Q. *J. Solid State Chem.* **2009**, *182*, 807−812.

(21) Barroso, M.; Cowan, A. J.; Pendlebury, S. R.; Grätzel, M.; Klug, D. R.; Durrant, J. R. *J. Am. Chem. Soc.* **2011**, *133*, 14868−14871.

(22) Liou, F. T.; Yang, C. Y. *J. Electrochem. Soc.* **1982**, *129*, 342−345.

(23) Wang, Y. M.; Yu, T.; Chen, X. Y.; Zhang, H. T.; Ouyang, S. X.; Li, Z. S.; Ye, J. H.; Zou, Z. G. *J. Phys. D: Appl. Phys.* **2007**, *40*, 3925−3930.

(24) McDonald, K. J.; Choi, K. S. *Chem. Mater.* **2011**, *23*, 4863−4869.

(25) Zeng, S. Y.; Tang, K. B.; Li, T. W. *J. Colloid Interface Sci.* **2007**, *312*, 513−521.

(26) Berry, F. J.; Greaves, C.; Helgason, O.; McManus, J.; Palmer, H. M.; Williams, R. T. *J. Solid State Chem.* **2000**, *151*, 157−162.

(27) Shannon, R. D. *Acta Crystallogr.* **1976**, *32*, 751−767.

(28) Moulder, J. F.; Stickle, W. F.; Sobol, P. E.; Bomben, K. D. *Handbook of X-Ray Photoelectron Spectroscopy*; Physical Electronics Division, Perkin-Elmer Corp.: Eden Prairie, MN, 1992.

(29) http://srdata.nist.gov/xps/Default.aspx. Accessed May 2012.

(30) Galuska, A. A.; Uht, J. C.; Marquez, N. *J. Vac. Sci. Technol., A* **1988**, *6*, 110−123.

(31) Xu, G. P.; Ji, S. L.; Miao, C. H.; Liu, G. D.; Ye, C. H. *J. Mater. Chem.* **2012**, *22*, 4890−4896.

(32) Shaukatali, N. I.; Ingole, P. P.; Santosh, K. H. *ChemPhysChem* **2008**, *9*, 2574−2579.

(33) Wang, G. M.; Ling, Y. C.; Wheeler, D. A.; George, K. E. N.; Horsley, K.; Heske, C.; Zhang, J. Z.; Li, Y. *Nano Lett.* **2011**, *11*, 3503−3509.

(34) Windisch, C. F.; Exarhos, G. J. *J. Vac. Sci. Technol., A* **2000**, *18*, 1677−1681.

(35) Sikora, J.; Sikora, E.; Macdonald, D. D. *Electrochim. Acta* **2000**, *45*, 1875−1883.

(36) Klahr, B.; Gimenez, S.; Fabregat-Santiago, F.; Hamann, T.; Bisquert, J. *J. Am. Chem. Soc.* **2012**, *134*, 4294−4302.

(37) Brug, G. J.; Van Den Eeden, A. L. G.; Sluyters-Rehbach, M.; Sluyters, J. H. *J. Electroanal. Chem.* **1984**, *176*, 275−295.

(38) Harrington, S. P.; Devine, T. M. *J. Electrochem. Soc.* **2009**, *156*, C154−C159.

(39) Wijayantha, K. G. U.; Saremi-Yarahmadi, S.; Peter, L. M. *Phys. Chem. Chem. Phys.* **2011**, *13*, 5264−5270.

(40) Matsumoto, Y. *J. Solid State Chem.* **1996**, *126*, 227−234.